AMERICAN SCIENTIFIC PUBLISHERS

Science of Advanced Materials
Vol. 8, pp. 272–277, 2016
www.aspbs.com/sam

ARTICLE

Effects of Post-Annealing on the Electrical Properties of Sputter-Deposited SnO Thin-Film Transistors

Ju-Yeon Kim[1], ByungSeong Bae[1], and Eui-Jung Yun[2,*]

[1]*Department of Display Engineering, Hoseo University, Asan-City, Chungnam 336-795, Korea*
[2]*Department of Information and Communication Engineering, Hoseo University, Asan-City, Chungnam 336-795, Korea*

ABSTRACT

This study examined the effects of post-annealing on the electrical properties of tin oxide (SnO)-based thin-film transistors (TFTs) deposited by a more TFT-industry-compatible sputtering process from a SnO target. The TFTs, as-sputtered at room temperature and post-annealed at low temperatures (150 °C), exhibited ambipolar characteristics and symmetrical *p*- and *n*-type conductivity. For post-annealing in N_2 and air, the developed TFTs exhibited dominant *p*-type conduction in the range, 200–300 °C. This was attributed to the increases in acceptor-like tin oxynitride and *p*-type SnO phases for the N_2 and air environments, respectively. On the other hand, the TFTs post-annealed at 200 °C in O_2 revealed dominant *p*-type conductivity, whereas those annealed at higher temperatures showed ambipolar conductivity. This suggests that the incorporation of excess oxygen into the SnO channel layers forms *n*-type SnO_2 layers at temperatures greater than 200 °C, which leads to ambipolar behavior. After annealing at 300 °C in N_2, the sputter-deposited SnO TFTs operating in the sub-threshold region revealed the best *p*-type behavior, including a linear hole field-effect mobility of 25 cm^2/Vs, a sub-threshold swing of 0.02 V/decade, an on/off ratio of 6.62×10^3, and a threshold voltage of 0 V.

KEYWORDS: Ambipolar Characteristics, *p*-Type Oxide TFT, Tin Oxide, Post-Annealing, RF Sputtering.

1. INTRODUCTION

Oxide thin-film transistors (TFTs), such as amorphous In–Ga–Zn–O (a-IGZO) TFTs, have been investigated because of their possible fabrication at low-temperatures (e.g., room temperature (RT)) and fewer processing steps than poly-silicon (Si) TFTs.[1,2] Oxide TFTs can also be formed easily using a range of sputtering methods, whereas poly-Si TFTs are normally realized using more complex chemical vapor deposition (CVD) methods.[2,3] On the other hand, poly-Si TFTs can exhibit *n*- and *p*-type conductivity, while most oxide TFTs except for a few materials only show *n*-type conduction. Up to now, *p*-type oxide TFTs have been reported but their performance was unsatisfactory compared to *n*-type oxide TFTs.[4,5]

Among the *p*-type oxide TFTs reported, such as tin oxide (SnO),[2,4–7] cupric oxide (CuO),[7] cuprous oxide (Cu_2O),[8] and nickel oxide (NiO),[9] SnO TFTs[10–21] have received particular attention because of their high possibilities for obtaining high quality *p*-type oxide TFTs. Because pseudo-closed Sn 5*s* and O 2*p* orbitals have the closed energy levels for effective interactions, they can easily form more isotropic and delocalized hybridized orbitals and provide more effective hole transport to the VBM.[2,4–7,12–21] The conduction-type can be changed in SnO films depending on the valency of the Sn ion.[2] To realize *p*-type SnO TFTs, Sn^{2+} ions should exist in the SnO channels because Sn^{4+} ions form *n*-type SnO_2 films.

Until now, SnO films using an active layer in TFTs were prepared using several deposition methods, such as pulsed laser deposition,[4,5,11,13] evaporation,[10,20,22] radio-frequency (RF) sputtering,[2,12,14–19,23,24] and sol–gel processes.[21] In this study, *p*-type SnO-based TFTs were fabricated by a more TFT-industry-compatible sputtering process from a SnO target. The post-annealing conditions in different N_2, O_2, and air environments altered the electrical properties of the sputtered-deposited SnO TFTs dramatically.

2. EXPERIMENTAL DETAILS

SnO channel layers were deposited on 150-nm-thick SiO_2 films grown on (100) Si substrates from a SnO (99.999%, 2 inch diameter) target. The pure Ar gas (99.999%) was used as the reaction gas and the Ar flow rate was 22 sccm. The working pressure was fixed to 20 mTorr during

*Author to whom correspondence should be addressed.
Email: ejyun@hoseo.edu
Received: 9 December 2014
Accepted: 13 January 2015

deposition. The target-to-substrate distance was kept constant at 10 cm for all depositions. The substrate was rotated at 13.5 rpm and was unheated during deposition. The SnO target power was fixed at 100 W. The typical thickness of the SnO channel layers was approximately 30 nm.

To prepare the patterned source and drain electrodes, molybdenum (Mo) films were deposited on top of the SnO channel layers through a shadow mask by DC magnetron sputtering. The Ar flow rate was 20 sccm. The working pressure was fixed to 0.5 mTorr during deposition. The input voltage was fixed to DC 100 V. The thickness of the Mo electrodes was 150 nm. The width (W) and length (L) of the fabricated samples were 1500 μm and 650 μm, respectively. Figures 1(a) and (b) show a schematic cross-sectional view and a photographic top view, respectively, of the typical samples prepared in this study. As shown in Figure 1, the TFTs have a bottom gate and a top contact structure.

To observe the effects of post-annealing on the device properties of SnO-TFTs, post-annealing was carried out at 150–400 °C for 1 hr in a furnace for N_2 and air annealing, and in the chamber for O_2 annealing. The device characteristics of the SnO-based TFTs were measured at RT in a darkened probe box in air using two Keithley 2400 source meters at the DC voltage source and a Keithley 6485 picoammeter for the current measurements along with the corresponding software (Microsoft visual basic). The capacitances of the SiO_2 gate dielectric films were measured at RT using an Agilent 42854A precision LCR meter after forming Ohmic contacts with a 150-nm-thick Mo layer by DC sputtering.

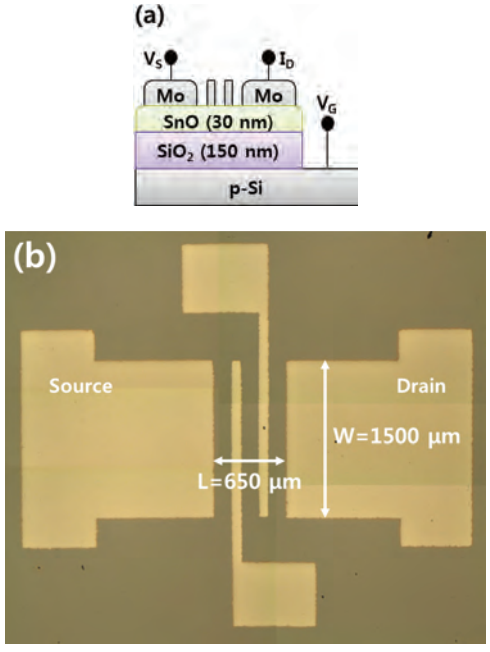

Fig. 1. (a) Schematic cross-sectional view and (b) photographic top view of sputter-deposited SnO-TFTs developed in this study: W = 1500 μm and L = 650 μm.

3. RESULTS AND DISCUSSION

Figure 2 shows the typical source-to-drain current versus the gate-to-source voltage (I_{SD}–V_{GS}) transfer curves of the sputter-deposited SnO-based TFTs before and after annealing at different temperatures in an oxygen (O_2) environment. A series of measurements were performed with the drain-to-source voltage (V_{DS}) fixed to −0.001 V, which is well within the sub-threshold region. The sub-threshold swing in the p-type operation (SS_p) for the same devices used in Figure 2 was also obtained from the inverse slope of the curve shown in Figure 2 using Eq. (1)[25, 26]

$$SS_p = \left[\frac{d(\log I_{SD})}{dV_{GS}}\right]^{-1} \quad (1)$$

Here, the sub-threshold swing in n-type operation (SS_n) can also be obtained if I_{SD} is replaced with I_{DS} in Eq. (1). If the device operates in sub-threshold mode, the linear hole field-effect mobility, $\mu_{\text{lin-hole}}$, in p-type operation can be calculated using Eq. (2)[27]

$$\mu_{\text{lin-hole}} = \frac{\partial I_{SD}}{\partial V_{GS}} \frac{L}{W} \frac{1}{C_{SiO_2}} \frac{1}{V_{SD}} \quad (2)$$

where C_{SiO_2} is the capacitance per area of the SiO_2 gate insulator, which was 23 nF/cm^2, as measured in a metal-insulator-metal configuration. The linear electron field-effect mobility, $\mu_{\text{lin-electron}}$, in the n-type operation can also be estimated using Eq. (2) if I_{SD} and V_{SD} are replaced with I_{DS} and V_{DS}, respectively. Table I lists the important device parameters of the sputter-deposited SnO-based TFTs, which were obtained from Figure 2 using Eqs. (1) and (2). Figure 3 also shows the characteristics of the important parameters, such as the linear mobility (μ_{lin}), on/off ratio ($I_{\text{on/off}}$) and sub-threshold swing (SS) at different post-annealing temperatures ($T_{\text{post-anneal}}$) in O_2 ambient obtained from Table I. As shown in Figures 2, 3, and Table I, the SnO-based TFTs as-deposited and

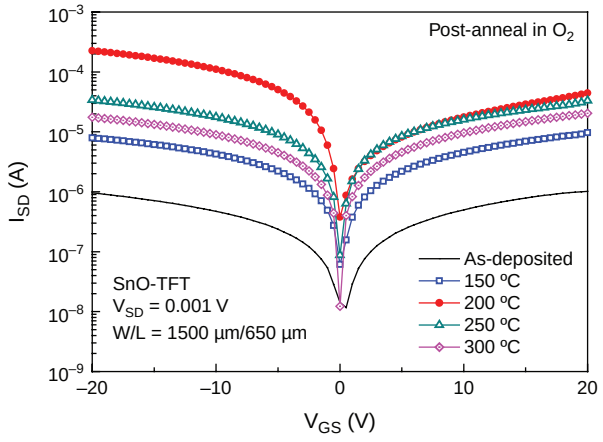

Fig. 2. Typical I_{SD}–V_{GS} transfer curves of sputter-deposited SnO-based TFTs after annealing at different temperatures in an oxygen environment. V_{DS} was fixed to −0.001 V, which is well within the sub-threshold region.

ARTICLE

Table I. Summary of the important device parameters of SnO-TFTs post-annealed in O_2, which were obtained from the results in Figure 2 using Eqs. (1) and (2).

Post-annealing Temperature in O_2 (°C)	V_{on} (V)	*p*-type parameter			*n*-type parameter		
		$\mu_{lin\text{-}hole}$ (cm^2/Vs)	$I_{on/off(p)}$	SS_p (V/dec.)	$\mu_{lin\text{-}electron}$ (cm^2/Vs)	$I_{on/off(n)}$	SS_n (V/dec.)
As-deposited (No annealing)	0.5	0.09	82.1	0.13	0.1	86.8	0.14
150	0	0.73	132	2.14	0.89	158	2.29
200	0	22.43	597	1.16	4.1	118	0.12
250	0	3.21	388	4.89	2.85	380	5.14
300	0	1.65	1.45×10^3	0.02	1.93	1.64×10^3	0.02

post-annealed at 150 °C in O_2 exhibited ambipolar properties, which have symmetrical *p*- and *n*-type parameters. The onset voltage (V_{ON}) (V_{ON}, defined as the source-gate voltage at which the mobile hole carriers begin to accumulate in the channel and the I_{SD} begins to increase in a transfer curve), reflecting the symmetry of an ambipolar TFT, is expected to be close to zero for an ambipolar TFT. Here, V_{ON} rather than the threshold voltage was used because V_{ON} is determined mainly by the trapped charges, whereas shifts in the threshold voltage in TFTs can be related to changes in many more physical parameters, such as the *SS* and mobility.[28,29] This suggests that in the SnO channel layers annealed at low temperatures, the number of *p*-type carriers originating from tin vacancies (V_{Sn}) and oxygen interstitials (O_i) is similar to that of *n*-type carriers resulting from tin interstitials (Sn_i) and oxygen vacancies (V_O).[2] Figure 3 clearly shows that $\mu_{lin\text{-}hole}$, $I_{on/off(p)}$ and SS_p, which are parameters in *p*-type operation, are more than five times greater than $\mu_{lin\text{-}electron}$, $I_{on/off(n)}$ and SS_n in *n*-type operation for SnO-based TFTs after annealing at 200 °C in O_2. This suggests that the SnO-TFTs post-annealed in O_2 at 200 °C exhibited dominant *p*-type unipolar behavior. Room temperature sputtered SnO_x films were reported[6] to show *p*-type conduction, which is originated mainly from V_{Sn}, presenting a polycrystalline structure composed of a mixture of tetragonal β-Sn and α-SnO_x phases, after annealing at 200 °C. Therefore, it was expected that the *p*-type conduction observed in these 200 °C post-annealed SnO-TFTs would be due to an enhancement of the V_{Sn} acceptors originating from the polycrystalline SnO-dominated channels. On the other hand, the TFTs annealed at higher temperatures in O_2 exhibited ambipolar operation once again. This suggests that the incorporation of excess oxygen into the SnO channel layers forms *n*-type SnO_2 layers and decreases the hole concentration at temperatures greater than 200 °C, which returns to ambipolar behavior. This result is consistent with a recent report on ambipolar behavior in SnO-TFTs post-annealed at 400 °C in an oxidative atmosphere.[2]

Figure 4 shows the typical I_{SD}–V_{GS} transfer curves of the sputter-deposited SnO-based TFTs, after annealing at different temperatures in air. The measurements were also carried out with a V_{DS} of −0.001 V. To analyze the result in Figure 4 more efficiently, the important parameters of μ_{lin}, $I_{on/off}$ and *SS* at different post-annealing temperatures ($T_{post\text{-}anneal}$) in an air ambient were deduced from Figure 4 using Eqs. (1) and (2), and their characteristics are shown in Figure 5. As shown in Figures 4 and 5, all balanced *p*- and *n*-type parameters were observed at $T_{post\text{-}anneal}$ = 200 °C, suggesting that ambipolar conduction occurred for the SnO-based TFTs post-annealed in air at 200 °C. Similar ambipolar TFTs were fabricated using a polycrystalline SnO channel layer deposited by electron-beam evaporation at RT, followed by rapid thermal annealing

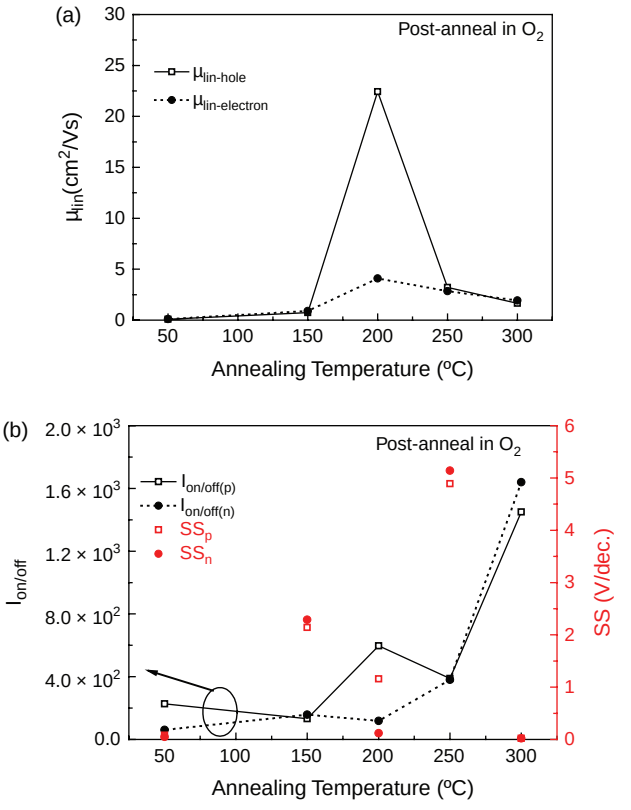

Fig. 3. Characteristics of the important parameters, such as (a) a linear mobility (μ_{lin}) and (b) an on/off ratio ($I_{on/off}$) and a sub-threshold swing (*SS*) at different post-annealing temperatures in an O_2 ambient obtained from Figure 2 and Table I. $\mu_{lin\text{-}hole}$, $I_{on/off(p)}$ and SS_p are the parameters in *p*-type operation and $\mu_{lin\text{-}electron}$, $I_{on/off(n)}$ and SS_n are parameters in *n*-type operation.

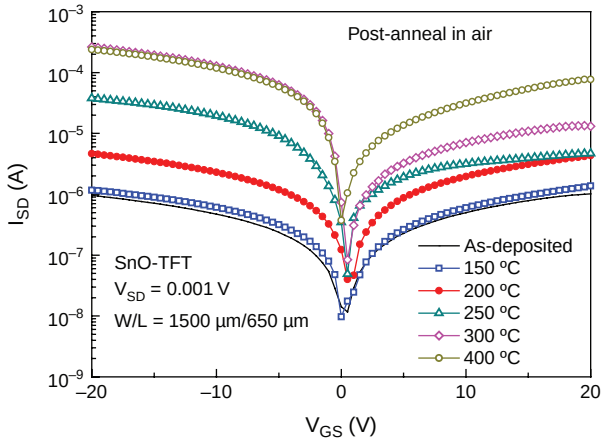

Fig. 4. Typical I_{SD}–V_{GS} transfer curves of sputter-deposited SnO-based TFTs after annealing at different temperatures in an air ambient. V_{DS} was fixed to −0.001 V, which is well within the sub-threshold region.

at 400 °C in Ar ambient.[30] In one study,[31] SnO_x TFTs fabricated by reactive rf magnetron sputtering of a Sn target at RT under an oxygen partial pressure (P_{O2}) of 11.8% and then annealed at 200 °C in an air ambient, exhibited weak ambipolar characteristic. Ambipolar operation was also observed[32] in reactive sputter-deposited SnO-TFTs using a Sn target at 90 °C and P_{O2} of 6.0% after annealing at 260 and 290 °C in air ambient. On the other hand, as shown in Figures 4 and 5, for 250 °C ≤ $T_{post\text{-}anneal}$ ≤ 300 °C, the $\mu_{lin\text{-}hole}$ and $I_{on/off(p)}$ *p*-type parameters for the SnO-TFTs sputter-deposited from a SnO target at RT and post-annealed in air showed an increasing trend (3.88–24.74 cm^2/Vs for $\mu_{lin\text{-}hole}$, 770–3110 for $I_{on/off(p)}$) with increasing $T_{post\text{-}anneal}$, whereas those *n*-type parameters change slightly. The ratio of *p*- to *n*-type parameters also increased with increasing $T_{post\text{-}anneal}$ in this region. Therefore, these sputter-deposited SnO-TFTs annealed in air exhibit *p*-type conduction, which is likely to be related to the increase in V_{Sn} in the polycrystalline SnO-dominated channels. Figure 4 also shows that as $T_{post\text{-}anneal}$ increases to 400 °C, the on source–drain current in the *p*-type characteristic (I_{SD} at $V_{GS} = -20$ V) did not change due to the unchanged $\mu_{lin\text{-}hole}$, whereas the on drain–source current in the *n*-type characteristic (I_{DS} at $V_{GS} = 20$ V) increased sharply owing to the large increase in $\mu_{lin\text{-}electron}$, as shown in Figure 5(a). Furthermore, the 400 °C post-annealed SnO-based TFTs exhibited near balanced *p*- and *n*-type parameters in $I_{on/off}$ and *SS*, as shown in Figure 5(b), suggesting that the TFTs annealed at a high temperature of 400 °C in air ambient show almost ambipolar characteristics due to compensation of the acceptors by the donors in the channel layer with a SnO–SnO_2 composite phase. This concurs with a recent report on ambipolar behavior in sputter-deposited polycrystalline SnO-TFTs after annealing at 400 °C in air.[2] One study[32] attributed the ambipolar operation in air-annealed SnO-TFTs at high annealing temperatures to the partial formation of a *n*-type SnO_2 channel.

Figure 6 presents the typical I_{SD}–V_{GS} transfer characteristics of the sputter-deposited SnO-based TFTs after annealing at various temperatures in a nitrogen (N_2) ambient. A very small $V_{DS} = -0.001$ V was applied to the TFT devices to investigate the device characteristics in

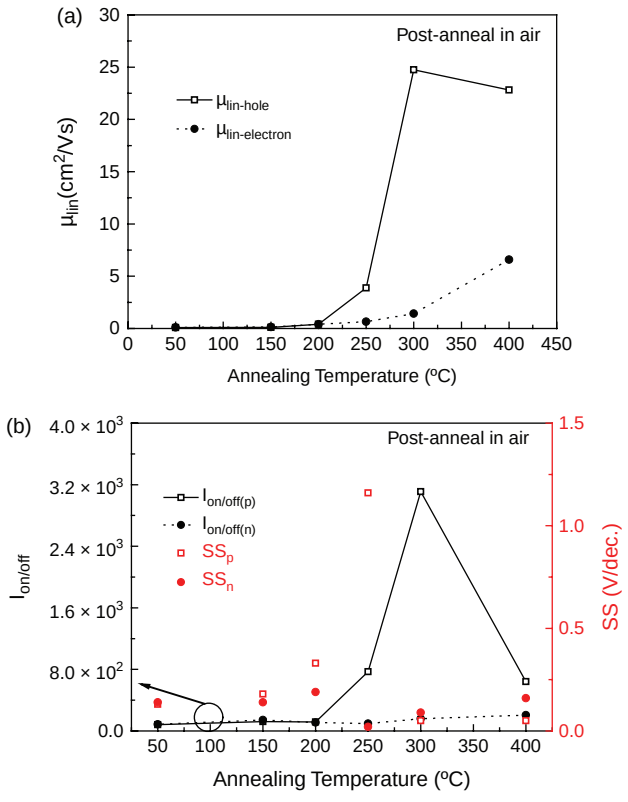

Fig. 5. Characteristics of the important parameters, such as (a) linear mobility (μ_{lin}) and (b) on/off ratio ($I_{on/off}$) and sub-threshold swing (*SS*) at different post-annealing temperatures in air ambient obtained from Figure 4. $\mu_{lin\text{-}hole}$, $I_{on/off(p)}$ and SS_p are parameters in *p*-type operation and $\mu_{lin\text{-}electron}$, $I_{on/off(n)}$ and SS_n are parameters in *n*-type operation.

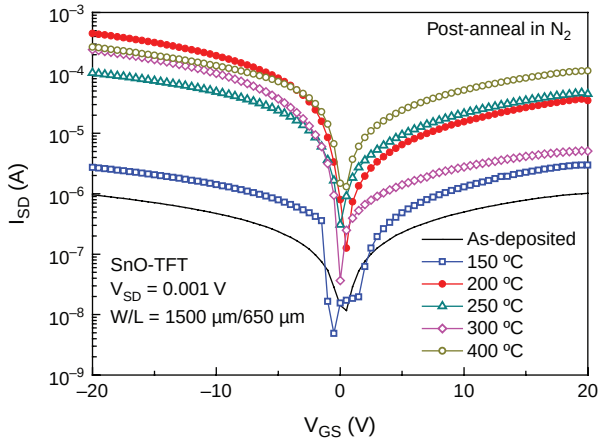

Fig. 6. Typical I_{SD}–V_{GS} transfer curves of sputter-deposited SnO-based TFTs after annealing at different temperatures in a nitrogen ambient. V_{DS} was fixed to −0.001 V, which is well within the sub-threshold region.

ARTICLE

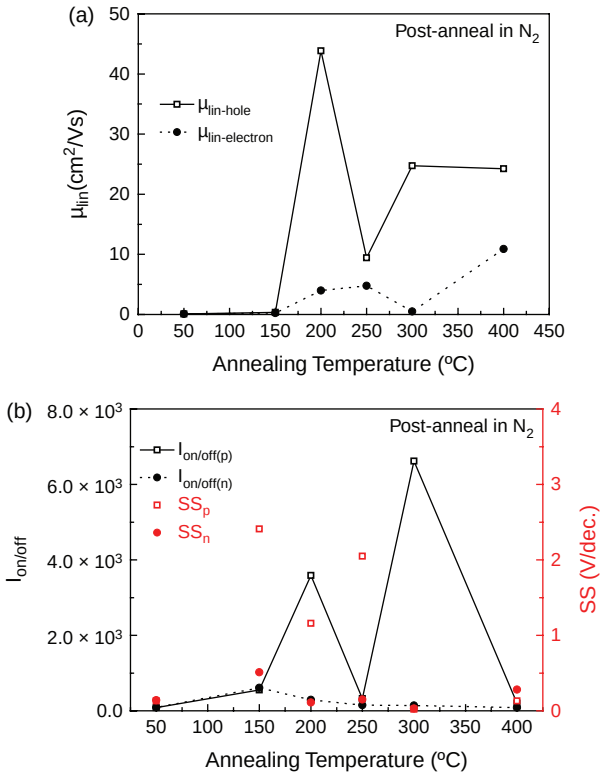

Fig. 7. Characteristics of the important parameters such as (a) linear mobility (μ_{lin}) and (b) on/off ratio ($I_{on/off}$) and sub-threshold swing (SS) at different post-annealing temperatures in a nitrogen ambient obtained from Figure 6. $\mu_{lin\text{-}hole}$, $I_{on/off(p)}$ and SS_p are parameters in p-type operation and $\mu_{lin\text{-}electron}$, $I_{on/off(n)}$ and SS_n are parameters in n-type operation.

the sub-threshold region. From the results in Figure 6, the important μ_{lin}, $I_{on/off}$ and SS parameters at different $T_{post\text{-}anneal}$ in a N_2 ambient were estimated using Eqs. (1) and (2), and their characteristics are plotted in Figure 7. As shown in Figures 6 and 7, near balanced p- and n-type parameters in μ_{lin} and $I_{on/off}$ were observed at a $T_{post\text{-}anneal} =$ 150 °C, suggesting that ambipolar conduction occurred for SnO-based TFTs post-annealed in N_2 at 150 °C. On the other hand, for post-annealing at 200 °C in N_2, $\mu_{lin\text{-}hole}$, $I_{on/off(p)}$ and SS_p in p-type operation (43.85 cm^2/Vs for $\mu_{lin\text{-}hole}$, 3590 for $I_{on/off(p)}$, and 1.16 for SS_p) were much greater than those in n-type operation (3.97 cm^2/Vs for $\mu_{lin\text{-}electron}$, 292 for $I_{on/off(n)}$, and 0.11 for SS_n). Furthermore, the $\mu_{lin\text{-}hole}$ to $\mu_{lin\text{-}electron}$ ratio and the $I_{on/off(p)}$ to $I_{on/off(n)}$ ratio were increased by post-annealing at 300 °C in N_2. Yabuta et al.[2] reported that the SnO-TFTs, which were fabricated by rf magnetron sputtering applying a SnO target at RT and then annealed at 300 °C in N_2, exhibited p-type characteristics due to the formation of p-type polycrystalline SnO channels. The p-type conduction of the N-doped SnO_2 channel layers grown by reactive sputtering at high N_2 partial pressure was attributed to atomic N incorporated substitutionally at the O sites to form tin oxynitride (SnON), which acts as an acceptor.[18, 23, 24, 33] Therefore, the SnO-TFTs annealed at 200 and 300 °C in N_2 present p-type conduction that is likely to be associated with an increase of acceptor-like SnON impurities formed by N atoms occupying the O sites in the polycrystalline SnO–SnO_2 channels. As $T_{post\text{-}anneal}$ was increased to 400 °C, the results in Figures 6 and 7 were similar to those in Figures 4 and 5. This suggests that the same argument used for the TFTs annealed at 400 °C in air can also be applied to those annealed at 400 °C in N_2.

The conversion from p-type characteristics to near ambipolar characteristics with $T_{post\text{-}anneal}$ observed for TFTs post-annealed at 400 °C in N_2 or air is believed to originate mainly from competition between the acceptor and donor generation process. In particular, for the p-type SnO-dominated channels, the majority carriers are holes resulting from acceptors, such as V_{Sn} and SnON impurities for air- and N_2-annealed TFTs, respectively. As the n-type SnO_2 content increases with $T_{post\text{-}anneal}$, the acceptors are gradually compensated for by the donors in the SnO_2. When the number of acceptors and the values of the p-type parameters have a similar order of magnitude as the donors and n-type parameters, the SnO_x channels would exhibit near ambipolar characteristics. Based on the experimental results, the best p-type SnO-based TFTs were obtained after annealing at 300 °C in N_2, which showed $\mu_{lin\text{-}hole} = 25$ cm^2/Vs, $I_{on/off(p)} = 6.62 \times 10^3$ and $SS_p = 0.02$ V/decade, and a threshold voltage of 0 V. Nitridation of the polycrystalline SnO–SnO_2 channels by N_2-annealing increased the hole density and finally produced p-type SnO channels. Note that the $\mu_{lin\text{-}hole}$ value is higher than that (6.75 cm^2/Vs) reported by Caraveo-Frescas et al.[34] for any p-type oxide TFTs.

4. CONCLUSION

This study examined the effects of post-annealing on the device properties of SnO-based TFTs fabricated by rf magnetron sputtering from a SnO target. Unannealed SnO-TFTs exhibited ambipolar properties, which have symmetrical p- and n-type parameters.

(1) For the TFTs post-annealed in O_2, they preserved ambipolar properties at 150 °C, suggesting that in the SnO channel layers annealed at low temperatures, the number of p-type carriers originating from V_{Sn} and O_i were similar to that of the n-type carriers resulting from Sn_i and V_O. On the other hand, the 200 °C post-annealed SnO-TFTs in O_2 exhibited dominant p-type behavior, which is due likely to an enhancement of the V_{Sn} acceptors originating from the polycrystalline SnO-dominated channels. After annealing at 300 °C in O_2, the TFTs showed ambipolar behavior because the incorporation of excess oxygen into the SnO channel layers forms n-type SnO_2 layers and decreases the hole concentration at high annealing temperatures.

(2) For the TFTs post-annealed in air, ambipolar, p-type and near ambipolar conductions were observed for $T_{post\text{-}anneal} = 200$ °C, 250 °C $\leq T_{post\text{-}anneal} \leq$ 300 °C and $T_{post\text{-}anneal}$ of 400 °C, respectively.

(3) For the TFTs post-annealed in N_2, ambipolar conduction occurred at $T_{post\text{-}anneal} = 150$ °C followed by *p*-type conduction at $T_{post\text{-}anneal} = 200$ and 300 °C.

The conversion from *p*-type conduction to near ambipolar conduction with $T_{post\text{-}anneal}$ observed for the TFTs post-annealed at 400 °C in N_2 or air originated from competition between the acceptor and donor generation process. For the *p*-type SnO-dominated channels, the V_{Sn} and SnON acceptor impurities are expected to be dominant for air- and N_2-annealed TFTs, respectively. When the number of acceptors and the *p*-type parameters have a similar order of magnitude as the donors and *n*-type parameters, the SnO_x channels would exhibit near ambipolar characteristics. The best *p*-type SnO-based TFTs were obtained after annealing at 300 °C in N_2, which showed $\mu_{lin\text{-}hole} = 25$ cm^2/Vs, $I_{on/off(p)} = 6.62 \times 10^3$, SS_p of 0.02 V/decade and a threshold voltage of 0 V. The $\mu_{lin\text{-}hole}$ value was higher than that reported to date for any *p*-type oxide TFTs.

Acknowledgments: This study was supported by the Academic Research Fund of Hoseo University in 2014 (FRC-2014-0082).

References and Notes

1. K. Nomura, H. Ohta, A. Takagi, T. Kamiya, M. Hirano, and H. Hosono, *Nature* 432, 488 (**2004**).
2. H. Yabuta, N. Kaji, R. Hayashi, H. Kumomi, K. Nomura, T. Kamiya, M. Hirano, and H. Hosono, *Appl. Phys. Lett.* 97, 072111 (**2010**).
3. H. Yabuta, M. Sano, K. Abe, T. Aiba, T. Den, H. Kumomi, K. Nomura, T. Kamiya, and H. Hosono, *Appl. Phys. Lett.* 89, 112123 (**2006**).
4. P.-C. Hsu, C.-C. Wu, H. Hiramatsu, T. Kamiya, and H. Hosono, *ECS J. Solid State Sci. Technol.* 3, Q3040 (**2014**).
5. Y. Ogo, H. Hiramatsu, K. Nomura, H. Yanagi, T. Kamiya, M. Hirano, and H. Hosono, *Appl. Phys. Lett.* 93, 032113 (**2008**).
6. E. Fortunato, R. Barros, P. Barquinha, V. Figueiredo, S.-H. K. Park, C.-S. Hwang, and R. Martins, *Appl. Phys. Lett.* 97, 052105 (**2010**).
7. S.-Y. Sung, S.-Y. Kim, K.-M. Jo, J.-H. Lee, J.-J. Kim, S.-G. Kim, K.-H. Chai, S. J. Pearton, D. P. Norton, and Y.-W. Heo, *Appl. Phys. Lett.* 97, 222109 (**2010**).
8. X. Zou, G. Fang, L. Yuan, M. Li, W. Guan, and X. Zhao, *IEEE Electron Device Lett.* 31, 827 (**2010**).
9. J. Jiang, X. Wang, Q. Zhang, J. Li, and X. X. Zhang, *Phys. Chem. Chem. Phys.* 15, 6875 (**2013**).
10. L. Y. Liang, Z. M. Liu, H. T. Cao, Z. Yu, Y. Y. Shi, A. H. Chen, H. Z. Zhang, Y. Q. Fang, and X. L. Sun, *J. Electrochem. Soc.* 157, H598 (**2010**).
11. Y. Ogo, H. Hiramitsu, K. Nomura, H. Yanagi, T. Kamiya, M. Hirano, and H. Hosono, *Phys. Status Solidi A* 206, 2187 (**2009**).
12. P.-C. Hsu, W.-C. Chen, Y.-T. Tsai, Y.-C. Kung, C.-H. Chang, C.-C. Wu, and H.-H. Hsieh, *Thin Solid Films* 555, 57 (**2014**).
13. K. Nomura, T. Kamiya, and H. Hosono, *Adv. Mater.* 23, 3431 (**2011**).
14. E. Fortunato, P. Barquinha, and R. Martins, *Adv. Mater.* 24, 2945 (**2012**).
15. J. Um, B. M. Roh, S. Kim, and S. E. Kim, *Mater. Sci. Semiconductor Process* 16, 1679 (**2013**).
16. P.-C. Hsu, W.-C. Chen, Y.-T. Tsai, Y.-C. Kung, C.-H. Chang, C.-J. Hsu, C.-C. Wu, and H.-H. Hsieh, *Jpn. J. Appl. Phys.* 52, 05DC07 (**2013**).
17. V. X. Hien, J.-H. Lee, J.-J. Kim, and Y.-W. Heo, *Sensor and Actuators B* 194, 134 (**2014**).
18. Y. Kim, J. H. Jang, J. S. Kim, S. D. Kim, and S. E. Kim, *Mater. Sci. Eng. B* 177, 1470 (**2012**).
19. T. Toyama, Y. Seo, T. Konishi, H. Okamoto, and Y. Tsutsumi, *Appl. Phys. Express* 4, 071101 (**2011**).
20. K. M. Abhirami, R. Sathyamoorthy, and K. Asokan, *Radiation Physics and Chemistry* 91, 35 (**2013**).
21. K. Okamura, B. Nasr, R. A. Brand, and H. Hahn, *J. Mater. Chem.* 22, 4607 (**2012**).
22. W. Guo, L. Fu, Y. Zhang, K. Zhang, L. Y. Liang, Z. M. Liu, H. T. Cao, and X. Q. Pan, *Appl. Phys. Lett.* 96, 042113 (**2010**).
23. S. S. Pan, G. H. Li, L. B. Wang, Y. D. Shen, Y. Wang, T. Mei, and X. Hu, *Appl. Phys. Lett.* 95, 222112 (**2009**).
24. Y. Kim, S.-P. Kim, S.-D. Kim, and S. E. Kim, *Current Appl. Phys.* 11, S139 (**2011**).
25. D. C. Paine, B. Yaglioglu, Z. Beiley, and S. Lee, *Thin Solid Films* 516, 5894 (**2008**).
26. K. M. Yu, J. T. Yuh, S. H. K. Park, M. K. Ryu, E. J. Yun, and B. S. Bae, *Jpn. J. Appl. Phys.* 52, 10MA12 (**2013**).
27. L. Schulz, E. J. Yun, and A. Dodabalapur, *Appl. Phys. A* 115, 1103 (**2014**).
28. M. Debucquoy, S. Verlaak, S. Steudel, K. Myny, J. Genoe, and P. Heremans, *Appl. Phys. Lett.* 91, 103508 (**2007**).
29. J. K. Choi, J. M. Song, K. M. Yu, B. S. Bae, and E. J. Yun, *J. Korean Phys. Soc.* 63, 2281 (**2013**).
30. L. Y. Liang, H. T. Cao, X. B. Chen, Z. M. Liu, F. Zhuge, H. Luo, J. Li, Y. C. Lu, and W. Lu, *Appl. Phys. Lett.* 100, 263502 (**2012**).
31. H. Luo, L. Y. Liang, Q. Liu, and H. T. Cao, *ECS Journal of Solid State Science and Technology* 3, Q3091 (**2014**).
32. I.-T. Cho, M. U, S.-H. Song, J.-H. Lee, and H.-I. Kwon, *Semicond. Sci. Technol.* 29, 045001 (**2014**).
33. Y. R. Kim, J. Um, S. D. Kim, and S. E. Kim, *ECS Solid State Letters* 1, P29 (**2012**).
34. J. A. Caraveo-Frescas, P. K. Nayak, H. A. Al-Jawhari, D. B. Granato, U. Schwingenschlögl, and H. N. Alshareef, *ACS Nano* 7, 5160 (**2013**).

ARTICLE